PNAS RESEARCH ARTICLE | EARTH, ATMOSPHERIC, AND PLANETARY SCIENCES

On the role of small estuaries in retaining buoyant particles

Tong Bo[a,b,1], David K. Ralston[a], W. Rockwell Geyer[a], and James C. McWilliams[b]

Edited by Andrea Rinaldo, Ecole Polytechnique Federale de Lausanne, Lausanne, Switzerland; received January 22, 2024; accepted July 22, 2024

Estuaries, as connectors between land and ocean, have complex interactions of river and tidal flows that affect the transport of buoyant materials like floating plastics, oil spills, organic matter, and larvae. This study investigates surface-trapped buoyant particle transport in estuaries by using idealized and realistic numerical simulations along with a theoretical model. While river discharge and estuarine exchange flow are usually expected to export buoyant particles to the ocean over subtidal timescales, this study reveals a ubiquitous physical transport mechanism that causes retention of buoyant particles in estuaries. Tidally varying surface convergence fronts affect the aggregation of buoyant particles, and the coupling between particle aggregation and oscillatory tidal currents leads to landward transport at subtidal timescales. Landward transport and retention of buoyant particles is greater in small estuaries, while large estuaries tend to export buoyant particles to the ocean. A dimensionless width parameter incorporating the tidal radian frequency and lateral velocity distinguishes small and large estuaries at a transitional value of around 1. Additionally, higher river flow tends to shift estuaries toward seaward transport and export of buoyant particles. These findings provide insights into understanding the distribution of buoyant materials in estuaries and predicting their fate in the land–sea exchange processes.

estuaries | ocean | buoyant particle transport | surface fronts

Significance

Understanding buoyant particle transport in estuaries is crucial for predicting the land–sea exchange of materials. In the traditional view, estuaries are expected to primarily export buoyant particles to the ocean. However, our study reveals a transport mechanism that traps buoyant materials within estuaries. This transport mechanism is based on flow characteristics common to many estuarine environments, making it broadly applicable. Crucially, we found that the retention of buoyant particles depends on estuarine geometry, with trapping more likely to occur in small estuaries compared to large estuaries. This underscores the need for increased attention to small estuaries regarding the impacts of buoyant pollutants, such as floating plastics or oil spills, and the dispersal of surface-oriented larvae of marine organisms.

Estuaries, as connectors between land and ocean, play a vital role in the ecosystem by facilitating nutrient cycling, carbon storage, and productive habitat (1–3). Estuaries are also focal points for anthropogenic impacts, e.g., dredging, shoreline modifications, and pollutant emissions with ports and population centers (4). The dynamics of estuaries, along with the associated physical and biogeochemical transport processes, are primarily controlled by the interplay of bidirectional tidal currents and river discharge. At subtidal timescales, estuarine flow is characterized by the superposition of continuous seaward river flow and depth-dependent estuarine exchange flow (5, 6). The estuarine exchange flow, also referred to as estuarine circulation, typically features a net seaward current near the surface and a net landward current near the bottom, driven by density gradient between freshwater and seawater.

The combined influence on near-surface velocity of seaward river flow and seaward estuarine exchange flow is typically expected to result in seaward transport of buoyant materials, which are mainly concentrated on the sea surface or within the upper water column. This implies the export of various buoyant materials into the ocean, such as organic matter, surface-oriented larvae, floating plastics, and oil spills (7–10). In contrast, the landward estuarine exchange flow near the bottom typically leads to the retention of sinking materials, e.g., sediment and the formation of an estuarine turbidity maximum (11).

While the mean estuarine exchange flow suggests export of buoyant materials from inland systems to the ocean, the complexity of small-scale and transient flow patterns can lead to Lagrangian transport that deviates from the mean Eulerian flow field. For example, surface fronts are transient, localized features that are commonly observed in estuaries (12, 13). Surface fronts are typically characterized by strong horizontal convergence due to the baroclinicity from the density gradient between water masses (13–15). The convergence at surface fronts thus directly impacts the aggregation and trapping of surface particles (8, 16) (Fig. 1). Moreover, estuarine fronts are transient features that vary on tidal timescales. While the short-term aggregation of pollutants and larvae associated with surface fronts has been extensively documented (7, 8, 16–18), their long-term impact on land–sea exchange processes, which ultimately determines the fate of these materials, remains less understood.

Rivers have been identified as primary sources of marine plastics (8, 19–22), but the role of estuaries in the pathways for plastics from land to the ocean is less clear (23–25). Estuaries may either act as sources or sinks of plastics depending on estuary type (26, 27). Recent observations have revealed the retention of floating plastics in many

Author affiliations: [a]Applied Ocean Physics and Engineering Department, Woods Hole Oceanographic Institution, Woods Hole, MA 02543; and [b]Department of Atmospheric and Oceanic Sciences, University of California Los Angeles, Los Angeles, CA 90095

Author contributions: T.B. and D.K.R. designed research; T.B., D.K.R., W.R.G., and J.C.M. performed research; T.B. contributed new analytic tools; and T.B., D.K.R., W.R.G., and J.C.M. wrote the paper.

The authors declare no competing interest.

This article is a PNAS Direct Submission.

[1]To whom correspondence may be addressed. Email: tbo@atmos.ucla.edu.

Published August 19, 2024.

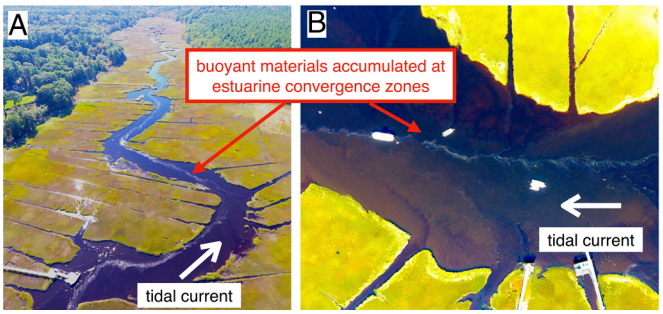

Fig. 1. Drone imagery of estuarine surface convergence fronts and the accumulated buoyant materials in the North River estuary (MA, USA). (*A*) Overview of an estuarine channel. (*B*) Detailed view of the surface convergence zone.

estuaries, suggesting that estuaries can slow the seaward transport or act as reservoirs for plastics (28–30), but the mechanism of this retention is not well understood. Similarly for biological transport, estuaries have been reported to either retain or export surface-oriented larvae (9, 18). Physical processes depending on the estuarine dynamics are thought to influence the distribution of larvae along with effects of their own active movement (31). In addition, near-surface organic matter may either accumulate within estuaries or be exported to the ocean (32, 33), which has significant implications for blue carbon sequestration. Therefore, conducting a more comprehensive investigation into the physical mechanisms governing buoyant particle transport in estuaries is essential for advancing our understanding of the land–sea exchange process across various research areas.

In this study, we use a combination of idealized numerical simulations, realistic numerical simulations, and a theoretical model to characterize factors affecting the fate of surface-trapped buoyant particles in estuaries. Our study aims to bridge the gap between intricate small-scale and transient processes such as surface convergence fronts that efficiently aggregate particles and the longer-term transport processes affecting the fate of buoyant materials.

Results

Contrasting Surface Particle Transport Directions in Two Realistic Estuaries. We conducted surface-trapped particle release experiments in hydrodynamic simulations of two different estuaries—the North River (MA, USA) and Delaware Bay (USA) (see *Materials and Methods* for details). The North River estuary is a relatively small tidal channel located on the New England coast of the United States (Fig. 2*A*). The channel width is 50 to 200 m and the thalweg depth is 3 to 8 m, and the salinity intrusion length extends landward from the mouth up to 20 km (34, 35). Delaware Bay is a considerably larger estuary located on the Mid-Atlantic coast of the United States (Fig. 3*A*), with an estuary width on the order of 1 to 10 km, a thalweg depth of 15 to 20 m, and a salinity intrusion length of over 100 km (36, 37). The vastly different sizes of the North River estuary and Delaware Bay allow us to examine buoyant particle transport in end-members representative of small and large estuaries.

Both estuaries are dominated by semidiurnal tides with a period of around 12.5 h. The mean seaward velocity due to the river flow is generally much weaker than the tidal velocity for both estuaries, with mean river velocities on the order of 0.01 m/s and tidal velocities of around 0.5 to 1 m/s. The major impact of river flow on estuarine dynamics arises from the freshwater input that creates horizontal salinity gradients and then generates the estuarine circulation, rather than any direct alteration to the tidal velocity field. This is a typical characteristic of estuarine fluid dynamics (5, 6).

In the North River estuary model, surface particles are released near the estuary mouth in the channel center, during a spring tide and a period of relatively low river discharge (Fig. 2*A*). Tidal amplitude is approximately 1.5 m and tidal velocities are around 0.5 m/s; the mean river velocity is ∼0.01 m/s. The along-estuary transport of surface-trapped particles generally reflects the bidirectional tidal current, i.e., landward during flood tides and seaward during ebb tides, as illustrated by the tidal fluctuations in Fig. 2*C*. However, at subtidal timescales particles exhibit a net landward transport, approaching the limit of the salt intrusion after several tidal cycles (Fig. 2 *A*, *C*, and *D*). The maximum distance that the particles' center of mass can reach is where the tidal-maximum surface salinity is about 2 psu, i.e., approximately 15 km into the estuary. The particle locations are distributed along-channel around their center of mass with a SD of ∼1 km, as a result of horizontal shear dispersion (38).

In addition to the particle release experiment presented in Fig. 2, other experiments involving different release locations or tidal conditions consistently demonstrate net landward transport of surface particles and eventual trapping inside the estuary at the salt intrusion limit after multiple tidal cycles. The tidally mean velocity is seaward near the surface with a magnitude of around 0.05 to 0.1 m/s in the mid-estuary region, due to the combined influence of river flow and estuarine exchange flow. This is expected to lead to seaward particle transport of ∼2 to 4 km over one tidal cycle. Nevertheless, the landward transport of surface-trapped particles in the North River estuary differs from the anticipated export of buoyant particles into the ocean, as inferred from the mean Eulerian flow. It is also worthwhile to note that the net landward transport is remarkably efficient, with the particle center of mass moving landward by up to ∼5 km over one tidal cycle, i.e., comparable to half of the tidal excursion distance.

The transport and fate of particles within the North River estuary experiments relates to the formation of surface fronts. During the flood tide, surface convergence fronts near the middle of the channel occur at multiple locations along the estuary (39). The buoyant particles accumulate at these fronts due to the surface convergence while being transported landward by the flood tide current (Fig. 2*B*, also see the drone imagery in Fig. 1). In contrast, during the ebb tide, surface fronts are less prevalent except for a buoyant plume front outside the estuary mouth. Consequently, buoyant particles typically remain near the channel banks when being transported seaward during the ebb tide, rather than aggregating at fronts in the middle of the channel. The asymmetry in the prevalence of fronts between flood and ebb tides is often found in estuaries due to differential interaction of the oscillatory tidal currents with the mean along-estuary salinity gradient (12, 40), as discussed more below. This tidal asymmetry in frontogenesis and particle aggregation serves as a significant contributor to subtidal landward transport, as will be demonstrated in the subsequent analysis of idealized simulations.

In the Delaware Bay simulations, subtidal transport of surface particles is seaward (Fig. 3), in contrast to the landward transport found in the North River estuary. Particles released at around 110 km into the estuary, corresponding to a salinity of 5 psu, are preferentially transported toward higher salinity regions farther seaward. This behavior remains consistent across various release experiments started from different locations or under different forcing conditions. The example release experiment shown in Fig. 3 is during a low river discharge period and has a mean river velocity of ∼0.01 m/s near the release region, which is comparable to the North River case. Surface fronts also occur in the Delaware

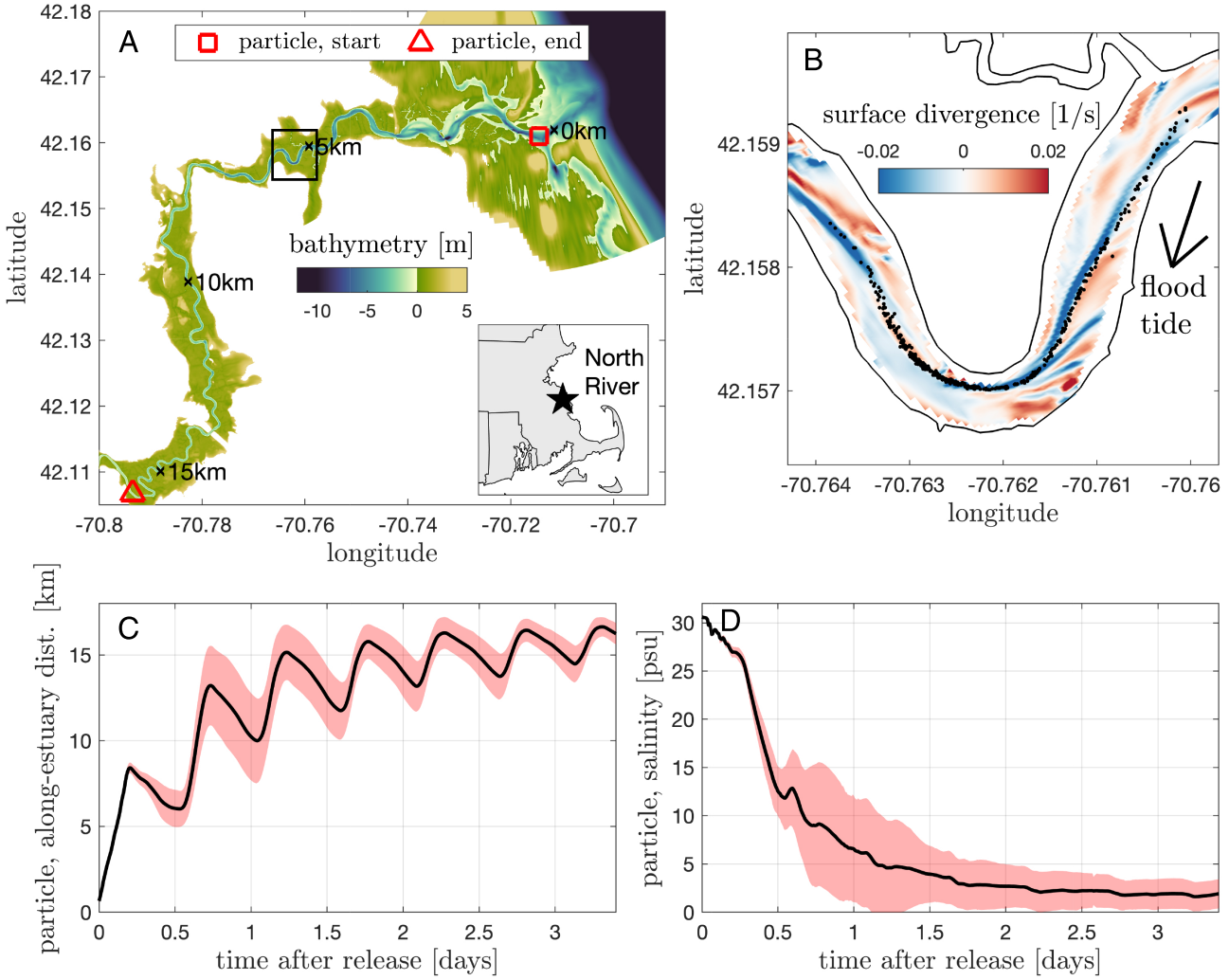

Fig. 2. North River estuary surface particle release experiment. (*A*) North River estuary model bathymetry. The average start and end locations of released surface particles after 3 d are indicated by a rectangle and triangle, respectively. (*B*) Snapshot during the flood tide, focusing on the region corresponding to the black rectangle in (*A*). Colors represent divergence of the surface velocity field, with blue indicating convergence zones. Particles are shown as black dots. (*C*) Along-estuary location of particles as a function of time after release. The black line denotes the average, and red shading shows the SD. (*D*) Salinity at particle locations.

and are more extensive during the flood tide than during the ebb. Particles in the Delaware simulations aggregate at these surface convergence fronts during the flood tide (Fig. 3*B*). Yet despite the similarities in the forcing conditions and the aggregation at surface front, the net transport of particles after multiple tidal cycles in Delaware Bay is seaward, opposite of that in the North River estuary. Note that in the North River simulations, particles released in the up-estuary region are eventually trapped at the landward salt intrusion extent, similar to those released near the mouth. The contrasting behavior in the long-term surface particle transport indicates fundamental differences in the trapping of buoyant materials in these estuaries of different size.

Velocity Field and Surface Convergence in the Idealized Models. To investigate the mechanisms behind the differences in trapping of surface-oriented particles between the two estuaries, we conducted a series of idealized estuary simulations (see details in Table 1). The idealized models have straight channels with widths ranging from 60 to 2,000 m and covarying depths of ~5 to 20 m, representing a spectrum from small to large estuaries. The models are forced by semidiurnal tides with 1-m amplitude, which drives tidal currents of around 0.5 m/s in the estuary, and constant river flow corresponding to a velocity of 0.002 to 0.05 m/s depending on channel width.

We selected two of the idealized models for detailed analysis, i.e., the 200-m wide model and 2,000-m wide model, which have similar dimensions to the North River estuary and Delaware Bay, respectively. Note that the Delaware Bay features a converging channel that varies in width from over 10 km wide near the mouth to approximately 1km in the up-estuary region. The 2,000-m width of the idealized model aligns with the up-estuary region of Delaware Bay, where the surface particles are released. While wide shallow shoal areas exist in lower Delaware Bay, the deep main channel is about 2,000-m wide to within 30 km of the mouth.

We first present the flow patterns in the idealized simulations (Fig. 4) before conducting a detailed analysis of processes behind the net surface particle transport. The subtidal velocity in the idealized model is seaward near the surface and landward near the bottom (Fig. 4*A*), consistent with the classical estuarine exchange flow.

During the flood tide, saltier seawater intrudes into the estuary due to advection by the landward tidal current. Typically, the tidal current is faster in the channel center and slower near

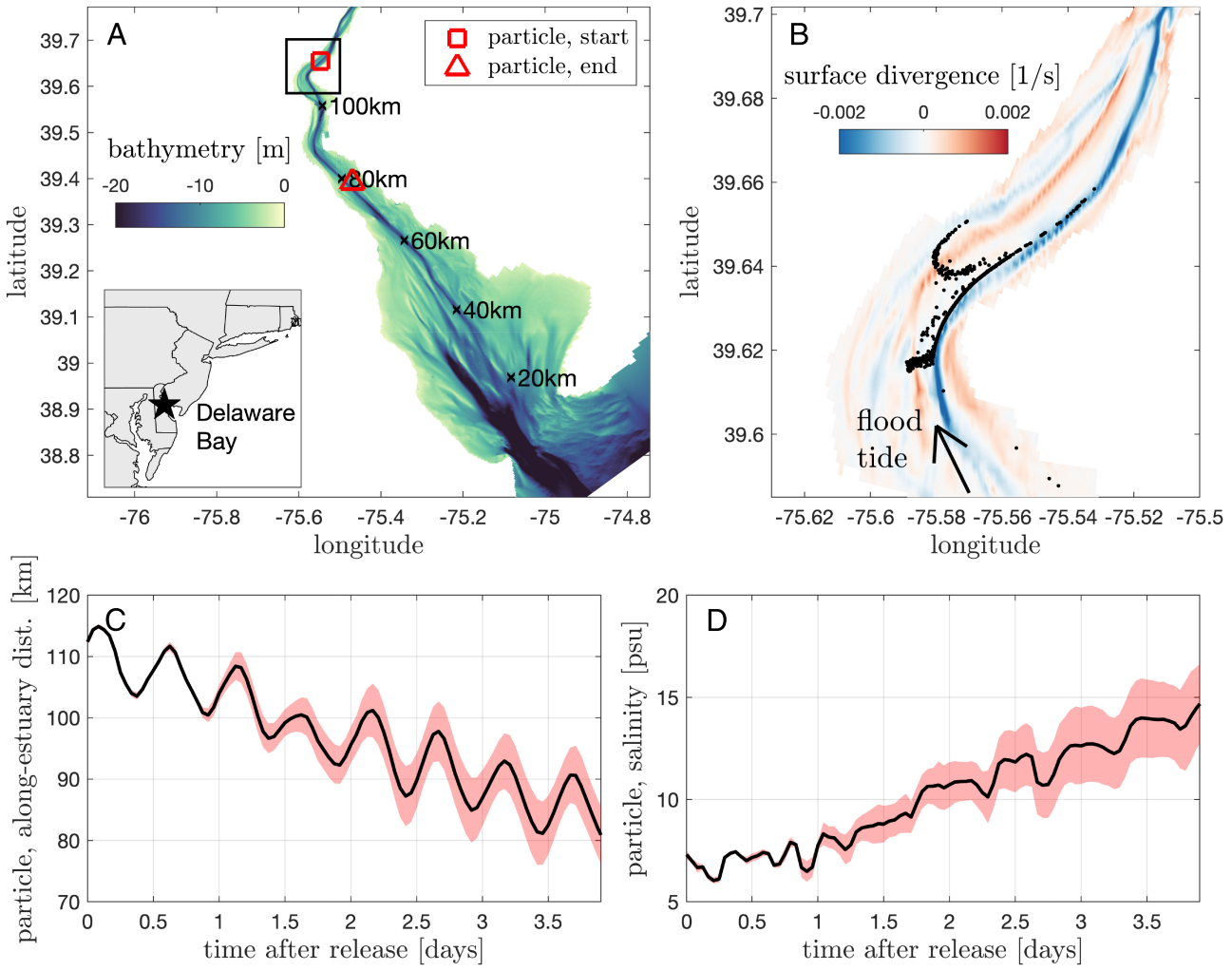

Fig. 3. Delaware Bay surface particle release experiment. (*A*) Delaware Bay model bathymetry. The average start and end locations of released surface particles after 3 d are indicated by a rectangle and triangle, respectively. (*B*) Snapshot during the flood tide, focusing on the region corresponding to the black rectangle in (*A*). Colors represent divergence of the surface velocity field, with blue indicating convergence zones. Particles are shown as black dots. (*C*) Along-estuary location of particles as a function of time after release. The black line denotes the average, and red shading shows the SD. (*D*) Salinity at particle locations.

the banks. This is because the channel depth is smaller near the banks, resulting in greater hydrodynamic drag from bottom friction (38, 41). As a result, the faster currents transport saltier water farther landward in the channel compared to the areas near the banks (Fig. 4 *B* and *D*). This creates lateral (across-estuary) salinity gradients and is commonly referred to as differential advection (6, 12, 41–43). The lateral density gradients give rise to counterrotating lateral circulation cells through baroclinicity, a widely observed feature in well-mixed and weakly stratified estuaries (12), resulting in converging lateral velocity near the surface toward the middle of the channel (Fig. 4*F*). Consequently, a surface convergence front is formed near the channel centerline and surface-oriented particles accumulate in the front. The occurrence of surface convergence during the flood tide in the models is observed in many estuaries (12, 16, 39, 44–46).

During the ebb tide, the faster seaward current in the channel center tends to transport fresher water farther seaward than on the adjacent shoals (Fig. 4 *C*, *E*, and *G*). Lower salinity is thus found in the middle of the channel compared to the regions near the banks. In contrast to the flood tide, the lateral density gradients resulting from differential advection during the ebb drive counterrotating lateral circulation cells with laterally divergent surface flow in the middle of the channel.

The 200-m wide model is presented in Fig. 4 for illustration but the other models have similar flow patterns. More generally, lateral baroclinic circulation due to differential advection of the along-channel salinity gradient is observed in many estuaries (12, 45). The differential advection mechanism does not apply in regions landward of the salt intrusion and seaward of the estuary mouth due to the lack of strong salinity gradients. In large estuaries, a lag between the baroclinic response of the lateral circulation and tidal phase of the along-estuary currents may occur, as will be discussed later. Additionally, while the Coriolis effect can influence the lateral circulation patterns in some large estuaries (43, 47), the baroclinic effect analyzed here can still dominate the lateral transport in a large estuary like Delaware Bay (48).

The seaward subtidal velocity near the surface (Fig. 4*A*) would be expected to lead to net seaward transport of surface particles over many tidal cycles, but distinct differences in net transport of Lagrangian particles among the idealized models indicate that other factors contribute. The mechanism governing the differences in the direction of buoyant particle transport among the different idealized estuaries (Table 1) is associated with the flood-ebb asymmetry in surface convergence (Fig. 4 *F* and *G*), as will be further analyzed below.

Table 1. Idealized and realistic estuary model parameters

Model	Width W [m]	Depth [m]	Tides [m]	Q_r [m^3/s]	u_r [m/s]	v_1 [m/s]	$\Omega W/v_1$	Δu_1 [m/s]	u_0 [m/s]	Long-term surf. part. direction
60 m	60	3 to 7	1	2	0.01	0.02	0.4	0.30	0.11	Landward
200 m	200	3 to 7	1	6	0.01	0.06	0.5	0.25	0.09	Landward
600 m	600	10 to 15	1	40	0.01	0.09	0.9	0.40	0.14	Landward
600 m, low Q_r	600	10 to 15	1	8	0.002	0.10	0.9	0.42	0.13	Landward
600 m, high Q_r	600	10 to 15	0.8	200	0.05	0.04	2.1	0.43	0.30	Seaward
2,000 m	2,000	15 to 20	1	200	0.01	0.11	2.7	0.63	0.23	Seaward
NR, spring	50 to 200	3 to 8	1.5	3	0.015	0.13	0.1 to 0.2	0.28	0.08	Landward
NR, neap	50 to 200	3 to 8	1	2	0.01	0.12	0.1 to 0.2	0.22	0.06	Landward
DB, low Q_r	2,000 to 4,000	15 to 20	0.8 to 1	100	0.005	0.25	1.4 to 2.3	0.63	0.20	Seaward
DB, high Q_r	2,000 to 4,000	15 to 20	0.8 to 1	1,000	0.05	0.34	1.1 to 1.7	0.63	0.34	Seaward

The idealized numerical models have channel widths of 60 m, 200 m, 600 m, and 2,000 m. Different river forcing conditions are tested in the 600-m wide model. NR represents the North River estuary, and DB represents the Delaware Bay. River discharge is denoted as Q_r, with the corresponding velocity estimated as u_r. Here, W is channel width, Ω is the tidal radian frequency, and v_1 is the amplitude of surface lateral velocity. The term u_0 is the mean seaward surface streamwise velocity, and Δu_1 is the difference between the lateral maximum and minimum amplitudes of the tidally varying streamwise velocity. Note that v_1, u_0, and Δu_1 come from model outputs rather than being prescribed as forcing. Models with a gray background indicate seaward surface particle transport at subtidal timescales, while models without the gray background exhibit landward transport.

Surface Particle Transport in the Idealized Models. To illustrate the differences in net transport of buoyant particles we compare the idealized models with channel widths of 200 m and 2,000 m. In the smaller estuary, the distribution of surface particles shifted landward over several tidal cycles and was eventually trapped at the salt intrusion limit (Fig. 5*B*). Conversely, in the 2,000-m wide estuary, surface particles were transported seaward and exported into the ocean (Fig. 5*F*). These contrasting behaviors align with the realistic models of North River (Fig. 2) and Delaware estuaries (Fig. 3).

In the smaller idealized estuary (200-m wide), the particles oscillate in the along-estuary direction with the bidirectional tidal currents. Laterally, particles aggregate near the channel centerline during the flood tide (Fig. 5*A*) due to advection and surface convergence with the counterrotating lateral circulation (Fig. 4*F*). The accumulated particles move landward with the lateral maximum flood tidal currents in the middle of the channel. By contrast, during the ebb tide, surface particles advect laterally toward the channel edges due to the reversed lateral circulation cells (Fig. 4*G*). Consequently, the seaward transport during the ebb occurs in the region of minimum velocity near the channel banks (Fig. 4 *B* and *C*). Therefore, the mean landward velocity of particles during the flood tide exceeds their mean seaward velocity during the ebb (Fig. 5*D*).

The surface-oriented particles steadily move landward at the subtidal timescale until they reach the extent of salt intrusion where the baroclinic forcing of the lateral circulation goes away (Fig. 5 *B* and *C*). It is noteworthy that all across the channel the maximum amplitude of the Eulerian surface velocity is greater during the ebb than during the flood tide, which is consistent with the seaward near-surface estuarine exchange flow. However, the Lagrangian transport of particles asymmetrically samples the tidal current over the tidal cycle, experiencing faster landward velocity near the centerline during the flood tide and slower seaward velocity near the banks during the ebb tide.

In the larger idealized estuary (2,000-m wide), surface particles are advected toward the centerline during the flood tide, driven by similar lateral circulation and surface convergence (Fig. 5*E*). However, owing to the greater channel width and longer lateral advection timescale, it takes longer for particles to collect in the surface front along the centerline compared to the smaller estuary. Likewise, during the ebb tide, particles in the larger channel take longer to reach the channel banks than in the smaller channel. Consequently, tidal currents that particles sample are less asymmetric between the flood and ebb tides in the larger estuary. Seaward subtidal transport occurs when the Lagrangian result of asymmetric sampling of the tidal oscillatory motions due to lateral shear is less than the seaward Eulerian mean surface velocity (Fig. 5 *F* and *G*). In an extreme case where the estuary is wide enough and surface particles cannot reach the centerline

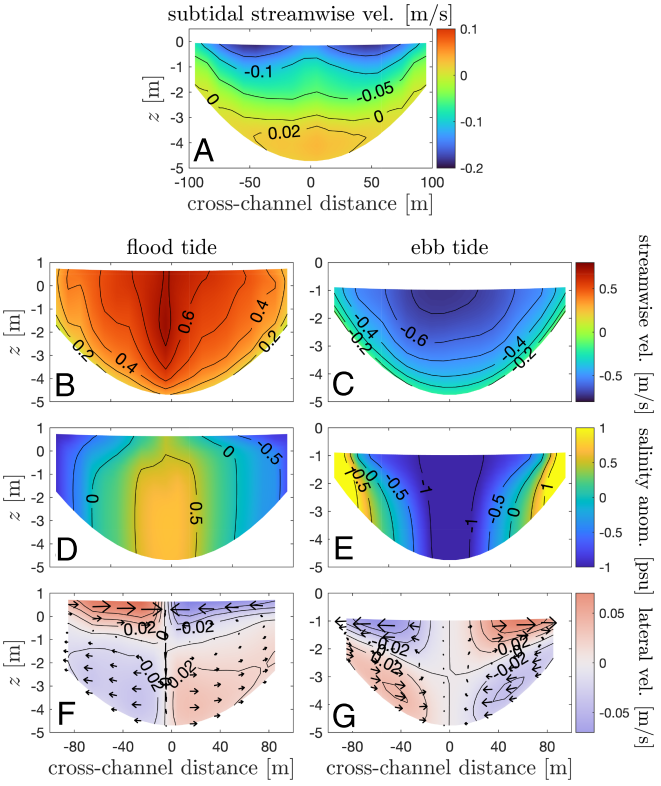

Fig. 4. Velocity and salinity fields of the 200-m wide idealized estuary model. (*A*) Subtidal streamwise velocity in a cross-section at 10 km into the estuary. Positive velocity indicates landward flow. (*B*) Streamwise velocity during the flood tide. (*C*) Streamwise velocity during the ebb tide. (*D*) Salinity anomaly, relative to the mean salinity of the cross-section, during the flood tide. (*E*) Salinity anomaly during the ebb tide. (*F*) Lateral velocity during the flood tide, with arrows showing lateral circulation. (*G*) Lateral velocity during the ebb tide. Note that the cross-section has a parabolic bed profile.

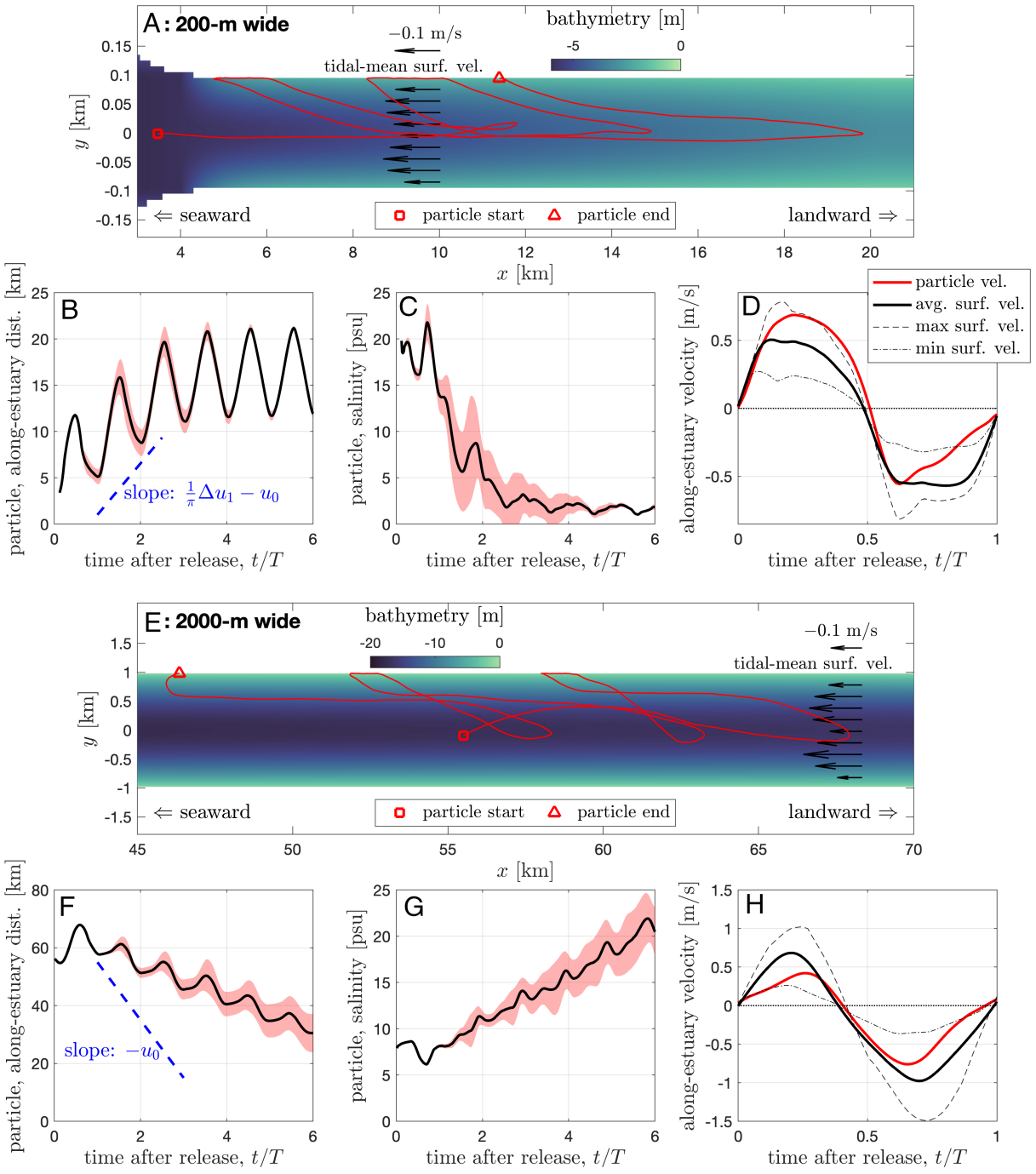

Fig. 5. Surface particle release experiments in the idealized numerical models. (*A*) Map view of a representative particle trajectory in the channel over three tidal cycles in the 200-m wide model. The rectangle and triangle indicate the start and end locations, respectively. Positive x indicates the landward direction. The black arrows show the tidal-mean Eulerian surface velocity, with negative values indicating the seaward direction. (*B*) Along-estuary location of surface particles as a function of time after release in the 200-m wide model. Time t is normalized by the tidal period T. The black line shows the average value of all particles and red shading indicates the SD. The dashed blue line indicates the maximum possible landward speed. (*C*) Salinity at particle locations in the 200-m wide model. (*D*) Average particle Lagrangian velocity over a tidal cycle in the 200-m wide model, compared with the lateral average, maximum, and minimum Eulerian along-estuary surface velocity. (*E*–*H*) Same as panels (*A*–*D*) but for the 2000-m wide model. The dashed blue line in (*F*) indicates the maximum possible seaward speed.

during the flood tide before the tidal current reverses direction, the asymmetric sampling effect disappears, and surface particles move seaward at a speed similar to the Eulerian mean surface velocity.

The differences in lateral advection and particle aggregation account for the contrasting subtidal transport behaviors in small and large estuaries. Similarly, the realistic North River estuary and Delaware Bay exhibit lateral circulation and particle transport processes that are consistent with the 200-m and 2,000-m wide idealized models, respectively, albeit with added complexity due to the realistic bathymetry. Overall, the findings in idealized and realistic simulations suggest that smaller estuaries facilitate more effective landward transport of surface particles and are more likely to trap buoyant materials. This trend is supported

by additional idealized simulation results (as shown in Table 1). Beyond channel width, forcing factors such as river flow and tidal amplitude can also influence net surface particle transport. These factors will be systematically investigated through a theoretical model in the subsequent section.

A Theoretical Model for Surface Particle Transport in Estuaries. A theoretical model is built to diagnose the buoyant particle transport behavior illustrated in the idealized and realistic estuaries. The theoretical model represents analytically key characteristics of estuaries, including oscillatory tidal currents, river flow and the associated along-estuary salinity gradients, differential advection of salinity gradients, and baroclinic lateral circulation (see details in *Materials and Methods*, Eqs. **6**, **7**, and **9**). The theoretical model identifies two primary dimensionless parameters that dictate the subtidal along-estuary transport of surface particles, namely, a dimensionless width $\Omega W/v_1$ and a dimensionless tidal-mean surface velocity $u_0/\Delta u_1$. Here, Ω is the tidal radian frequency, W is the channel width, and v_1 is the amplitude of the tidal surface lateral velocity, so $\Omega W/v_1$ also scales with the ratio of the lateral advection timescale to the tidal period. The dimensionless parameter $u_0/\Delta u_1$ compares the tidal-mean surface streamwise velocity u_0 to the lateral shear of the tidally varying streamwise velocity Δu_1 (the difference between the maximum and minimum tidal velocity amplitudes across the channel). In general, decreased $\Omega W/v_1$ and decreased $u_0/\Delta u_1$ favor the landward subtidal transport of surface-oriented particles in estuaries (Fig. 6).

The increased dimensionless width $\Omega W/v_1$ tends to shift an estuary from the landward transport regime to the seaward regime (Fig. 6*A*), because smaller estuaries are more effective in aggregating surface particles through lateral circulation and creating the flood-ebb asymmetry in Lagrangian transport (Fig. 6 *B* and *C*). The theoretical model results are consistent with the numerical simulations and generalize the proposed mechanism. In wide estuaries with a large $\Omega W/v_1$, the tidally averaged

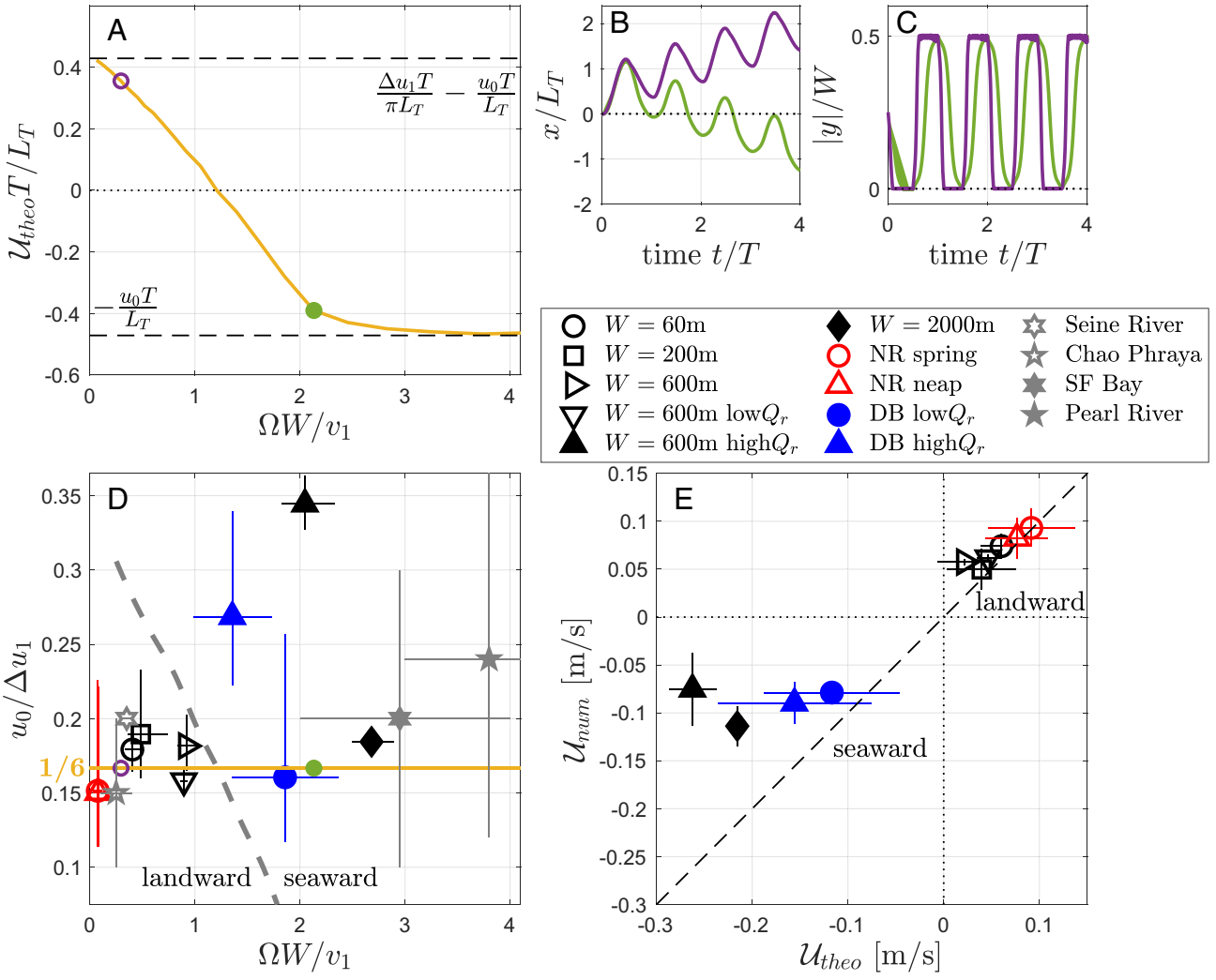

Fig. 6. Theoretical model of surface particle transport and its comparison with idealized and realistic numerical simulations. (*A*) Subtidal particle transport velocity $\mathcal{U}_{\text{theo}}$, normalized by the tidal period T and tidal excursion distance L_T. Here, $\mathcal{U}_{\text{theo}}$ is plotted as a function of $\Omega W/v_1$, for a representative value of $u_0/\Delta u_1 = 1/6$. (*B* and *C*) Along-estuary location and cross-channel distance to centerline from the theoretical particle transport model, as a function of time, for landward (purple) and seaward (green) transport scenarios. The landward and seaward transport scenarios correspond to the purple and green markers in (*A*), respectively. (*D*) Dependence of particle transport direction (landward or seaward) on $\Omega W/v_1$ and $u_0/\Delta u_1$. The gray line is obtained from the theoretical model, separating the landward and seaward transport regimes. The black, red, and blue points represent idealized and realistic numerical models. The gray points represent estimates from observational studies. Color-filled markers indicate seaward transport. See legend for details. The orange line corresponds to the representative scenario in (*A*). (*E*) Comparison of subtidal surface particle transport velocity in the numerical simulations ($\mathcal{U}_{\text{num}}$) with predictions from the theoretical model ($\mathcal{U}_{\text{theo}}$).

transport speed of surface particles asymptotes toward the mean Eulerian surface velocity $-u_0$, with the negative sign denoting the seaward direction. In narrow estuaries with a small $\Omega W/v_1$, the transport speed approaches $\Delta u_1/\pi - u_0$, an analytically derived value by assuming that surface particles fully sample the lateral maximum and minimum tidal velocity during the flood and ebb tides, respectively.

Decreased tidal-mean surface streamwise velocity u_0 and increased velocity difference between the channel center and banks (Δu_1) both favor the landward transport of surface particles. The lateral velocity difference Δu_1 is usually due to the lateral variability of channel bathymetry, i.e., lateral shear induced by the bottom frictional torque (38). Note that u_0 results from both the continuously seaward river discharge and the seaward subtidal estuarine exchange flow near the surface. The strength of estuarine exchange flow typically increases with river discharge and decreases with tidal mixing (5, 6). Therefore, higher river flow and weaker tides are expected to lead to the export of surface-oriented particles to the ocean. This effect is exemplified in the 600-m wide idealized models, where an increase in river flow and a decrease in tidal amplitude shift the estuary from a landward regime to a seaward regime for the same channel width (Table 1).

We estimated the two parameters, $\Omega W/v_1$ and $u_0/\Delta u_1$, for the numerical simulations discussed above. The predicted particle transport directions using the estimated dimensionless parameters in the theoretical model generally align with the simulation results (Fig. 6*D*). This agreement suggests that the flood-ebb asymmetry in surface convergence and the resultant asymmetry in Lagrangian along-estuary particle velocity, as captured by the simplified theoretical model, constitute a dominant mechanism in determining subtidal particle transport direction. Note that the dimensionless width $\Omega W/v_1$ typically has greater variability among different estuaries than the ratio $u_0/\Delta u_1$, which typically falling within the range of 0.1 to 0.2 except during high-discharge events. Beyond predicting transport direction, the theoretical model also provides reasonable estimates of the net transport velocity of surface particles in the landward regime (Fig. 6*E*). However, the theoretical model tends to overestimate the seaward particle transport velocity in large estuaries, indicating that other unaccounted factors influence particle transport, as will be discussed later.

Comparison with Observations. In this section, we compare the surface particle transport mechanism investigated in this study with observational results from other studies. Observational studies using buoyant drifter releases have found that in many estuaries the drifters are retained or move landward over multiple tidal cycles. For example, in a GPS-tracker study in the Seine estuary (France), floating bottles exhibited net landward transport over many tidal cycles (29). Notably, this net landward transport was observed only within the estuary region, not in the upstream tidal river, landward of salt intrusion. This suggests that the Seine estuary is retentive of buoyant materials, and is consistent with reported residence times for macroplastics of years in this estuary (28). The width in the region of the Seine where landward transport was observed is 200 to 300 m, corresponding with a dimensionless width parameter $\Omega W/v_1$ of 0.3 to 0.4 and $u_0/\Delta u_1$ of around 0.2 (49, 50). This aligns with the small estuary regime in this study (Fig. 6*D*). Another example comes from the Chao Phraya River estuary (Bangkok), where floating drifters released in the landward river were primarily retained near the salt intrusion limit rather than being exported into the ocean (51, 52). The channel is approximately 200 m wide where drifters are retained, with an estimated $\Omega W/v_1$ of 0.1 to 0.4 and $u_0/\Delta u_1$ of 0.1 to 0.2, consistent with the small estuary regime. In contrast, in larger estuaries such as the San Francisco Bay (USA) (53) and the Pearl River estuary (China) (54), surface drifters released in the estuary are transported into the ocean over multiple tidal cycles, aligning with the behaviors of surface particles in the large estuaries and Delaware Bay in this study. The estimated width parameter is $\Omega W/v_1 \approx 2$ to 4 for the San Francisco Bay, and $\Omega W/v_1 \approx 3$ to 5 for the Pearl River estuary, both falling within the large estuary regime.

The retention of buoyant materials in small estuaries has been widely documented in other studies. Examples include surface-oriented larvae in the Grays Harbor estuary (USA) (18), plastic drifters in the Waitemata estuary (New Zealand) (55), floating litter in the Pas estuary (Spain) (56), and microplastics near the salt intrusion extent of the Raritan River (USA) (57). The accumulation of buoyant particles in small estuaries, particularly floating plastics, has received increasing attention in recent observations. However, experimentally tracking drifters to evaluate transport pathways in estuaries over many tidal cycles poses logistical challenges (55, 58). Given the growing interest in these buoyant materials, it is crucial to conduct more drifter studies in small estuaries. In the meantime, measuring hydrodynamic conditions is recommended, as they significantly impact drifter transport.

One important factor influencing observational studies is particle stranding, especially for smaller-sized drifters or in intertidal zones subject to periodic inundation and drainage (29, 59, 60). The numerical results in this study do not include a specialized stranding and remobilization model to resolve the interaction between buoyant materials and channel banks or marsh vegetation (60, 61). The conclusions drawn from this study are therefore more applicable to scenarios where stranding does not occur over tidal cycles, such as with steep channel banks and for large particles like macroplastics and sea wrack (29, 30, 62, 63). Particle stranding typically occurs during ebb tides when lateral circulation advects buoyant materials toward the banks (55), and these particles may be remobilized during flood tides. Therefore, stranding is also expected to contribute to the flood-ebb asymmetry and net landward transport of surface particles in small estuaries, unless the stranded particles remain immobilized permanently.

Discussion

Smaller estuaries tend to result in the landward transport of surface particles over many tidal cycles through a mechanism involving the flood-ebb asymmetry of lateral circulation and surface convergence (Fig. 7). These findings underscore the potential of small estuaries to trap buoyant materials, whereas large estuaries are more likely to export them into the ocean. Specifically, the transport direction can be predicted by a dimensionless width $\Omega W/v_1$, where the estuary width is scaled by the lateral advection length-scale during the tidal cycle. Landward transport is expected when $\Omega W/v_1 < \sim 1$, and vice versa. The investigated trapping mechanism extends to applications in floating plastics and oil spill cleanup, as well as predictive modeling of the distribution of surface-trapped larvae or organic matter within estuaries. Additionally, high river discharge events may shift an estuary from the landward subtidal transport regime to seaward transport, particularly in estuaries of intermediate width. This suggests that heavy rainfall and river flooding can increase delivery of buoyant materials from the watershed

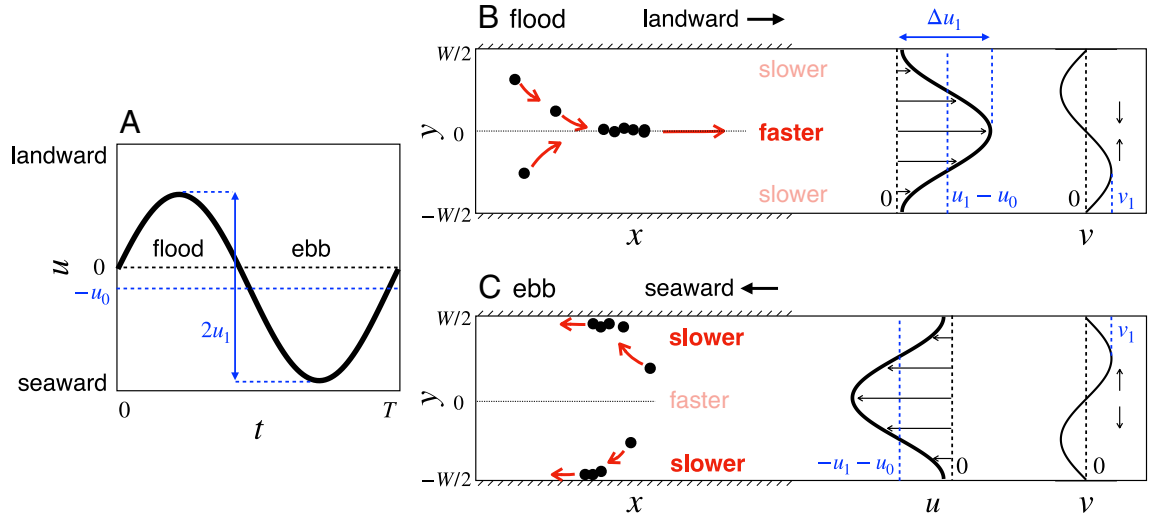

Fig. 7. Schematics of the net landward surface particle transport mechanism in small estuaries. (*A*) Surface streamwise velocity u over a tidal cycle. The laterally averaged mean seaward velocity is $-u_0$, and the amplitude of the tidally oscillatory component is u_1. (*B* and *C*) Schematics of surface particle transport (asymmetric sampling between flood and ebb tides), the lateral distribution of the surface streamwise velocity u, and surface lateral velocity v. (*B*) Maximum flood tide; (*C*) maximum ebb tide. Here, x is the along-estuary coordinate and y is the cross-estuary coordinate, with $y = 0$ denoting the channel centerline and $y = \pm W/2$ denoting the banks.

and subsequently enhance their export from estuaries into the ocean.

We have identified the dimensionless width and relative mean flow strength as two fundamental parameters influencing surface particle transport, but other factors also merit further investigation. The presence of complex topographic and bathymetric features, e.g., headlands, meanders, and side tributaries, can create sharp surface fronts that locally enhance particle aggregation (64–66). Wind stress is not considered here, but it can drive strong surface currents and influence the long-term transport of surface particles (67, 68). Wind can generate surface waves that induce long-term transport in the downwind direction through the Stokes drift (69, 70). Additionally, strong stratification in estuaries can alter the lateral circulation and modify patterns of surface convergence and the aggregation of surface particles (12, 43, 71, 72). Strong stratification is usually correlated with high river discharge (6). As a result, increased river flow can enhance particle export by increasing the mean seaward Eulerian velocity u_0 (Fig. 6*D*) while also reducing the tidally varying lateral velocity v_1 through increased stratification. Neap tides typically increase stratification and inhibit lateral circulation (43), thus weakening the surface particle trapping mechanism. However, the influence of spring-neap variability appears to be less dominant compared to other factors such as estuary geometry (width) and river discharge, as the typical range of spring-neap tides results in relatively small variations in the two fundamental parameters investigated in this study.

In large estuaries, the baroclinic response of lateral circulation may lag behind the oscillatory tidal current (see Eq. **12** in *Materials and Methods*), weakening the flood-ebb asymmetry in surface particle transport and further diminishing the trapping potential. The Coriolis effect can also impact subtidal estuarine circulation patterns (47) and the long-term transport of surface particles (73). A wide channel-shoal system can influence the lateral distribution of the residual circulation and modify Eulerian surface velocities, thereby affecting particle transport (74). These various factors may collectively explain the overestimation of particle transport velocity in large estuaries by the theoretical model, as shown in Fig. 6*E*. Moreover, large estuaries often contain multiple, smaller tributaries (subestuaries). While multiple-channel systems are not investigated in this study, it is noteworthy that buoyant particles may be retained within these small tributaries (58), even if the main estuary tends to export them into the ocean.

Furthermore, while we have focused on surface-trapped buoyant particles in this study, future research could explore a wider range of particle properties, e.g., from positively to negatively buoyant, to understand their long-term transport dynamics in estuaries (10, 46). Additionally, beyond passive particles, incorporating active particle motion would be relevant to larval transport (9).

Materials and Methods

North River Estuary Simulations. The North River estuary simulations are conducted using the Regional Ocean Modeling System (ROMS) (75–78), a free-surface hydrostatic model based on the Reynolds-averaged Navier–Stokes equations. The model domain extends from the Massachusetts Bay to approximately 20 km into the estuary, with an orthogonal curvilinear grid in the horizontal direction. The finest horizontal resolution is 3 m in the channel, with grid spacing increasing offshore and over the marsh areas away from the channel. The marsh areas have been masked out and excluded in this study to concentrate on channel dynamics and prevent marsh-induced particle trapping. A terrain-following coordinate with 16 uniformly distributed layers is used in the vertical direction. The k-ϵ closure of the generic length-scale turbulence closure scheme is used for the vertical mixing (79). A third-order upwind advection scheme is used for horizontal advection. The horizontal mixing coefficient is 0.01 m^2/s, which is consistent with scaling estimates based on velocity and water depth (38). No-slip boundary conditions are applied at the interior boundaries between the channel (unmasked grids) and banks (masked grids) in ROMS. Detailed information on the model setup, along with extensive comparisons with observational data, can be found in a previous study (80).

The simulations were run for a spring-neap cycle in early October in 2021. Tidal fluctuations on the ocean boundaries were extracted from the ADvanced CIRCulation (ADCIRC) database (81), with the amplitude varying between around 0.8 and 1.5 m. Subtidal fluctuations were obtained from the low-pass filtered water surface elevation record from the National Oceanic and Atmospheric Administration station at Boston (#8443970). River discharge was input as a freshwater source on the western boundary based on data from the U.S. Geological Survey gauge at Hanover (#01105730). The river discharge was

moderate to low during the simulation period and was generally less than 5 m^3/s, corresponding to a velocity of less than 0.02 m/s. Wind forcing was not included in the model.

Both tidal and river conditions have important impacts on estuarine dynamics and lateral circulation, consequently affecting particle transport. To exemplify this variability, here we provide a brief overview of the different tidal and river conditions in the North River estuary simulations. During spring tides, lateral circulation and surface convergence are generally stronger due to the increased tidal currents and weakened stratification. This is consistent with observations from the North River estuary (34, 39, 66). As a result, spring tides typically lead to more pronounced landward transport and trapping of surface particles. In contrast, during neap tides, stronger stratification and weaker lateral circulation lead to less effective aggregation of surface particles compared to spring tides. Nevertheless, net landward transport of surface particles still occurs because the North River estuary is well within the regime of small estuaries, making it less sensitive to tidal conditions. Additionally, high river discharge tends to increase stratification, inhibit lateral circulation, and increase the seaward Eulerian surface velocity, thereby weakening the trapping mechanism of surface particles.

Delaware Bay Simulations. The Delaware Bay simulations are also conducted using ROMS, with the model domain extending from the Atlantic Ocean to the head of tide at Trenton, New Jersey, approximately 190 km from the mouth. The curvilinear grid has a horizontal resolution of around 100 m, and 20 terrain-following layers are used in the vertical direction. Detailed description of the model setup and validation with observations can be found in previous studies (37, 48). The simulations were run with realistic tidal forcing from the ADCIRC tidal database. Freshwater discharge was input at Trenton, with two constant values representing the low and high river flow scenarios, 100 and 1,000 m^3/s, respectively. Wind forcing is not used in the model.

Idealized Estuary Simulations. A series of idealized estuary models are simulated using ROMS, featuring straight channel geometries with widths from 60 to 2,000 m (Table 1). The finest horizontal resolution varies between 3 and 40 m depending on the estuary width. The channels have parabolic cross-sections, with the thalweg depth ranging from 3 to 20 m and a minimum depth of 1.5 to 2 m near the banks. The models are forced by semidiurnal tides on the open ocean boundary, with a period of 12 h and an amplitude of 1 or 0.8 m. Constant river discharges of 2 to 200 m^3/s are input at the landward boundary, which corresponds to a moderate river flow of around 0.01 m/s in all the models. In the case of the 600-m wide estuary model, we conducted additional experiments with low and high discharge scenarios, characterized by river velocities of 0.002 and 0.05 m/s, respectively. The idealized models encompass a broad spectrum of estuary sizes, representing both small and large estuaries, such as the North River estuary and Delaware Bay. The Coriolis force is included in the models corresponding to mid-latitude conditions. The numerical mixing and advection schemes employed in these idealized models mirrored those used in the North River estuary model. Similar idealized estuary models have been used in previous studies (65, 82).

The Particle Tracking Model. Particle transport was modeled using ROMSPath (83), an offline particle tracking tool. In this study, we employed passive particles that remain at the surface. The particle motion was determined based on advection processes by the surface velocity field from the ROMS model outputs. Additionally, small random displacements of particles are incorporated to account for horizontal diffusion, calculated using a constant diffusion coefficient of 0.01 m^2/s that corresponds to the ROMS model settings. Particles were released near the channel centerline in the analyzed experiments. Sensitivity tests were conducted by releasing particles at various locations across the channel, which yielded consistent conclusions. The ROMS model output frequency is 10 min in the idealized simulations and the North River simulations, and 1 h in the Delaware Bay simulations. A sensitivity test was conducted in the 2-km wide idealized model, comparing the output frequencies of 10 min and 1 h, and the relative change in particle transport speed is less than 10%. In scenarios where particles are advected toward the bank, the outward lateral velocity in the flow field diminishes near the bank. In the meantime, horizontal mixing can induce a random walk that moves the particles away from the bank. Consequently, particles may not completely stick to the bank when transported close to it.

The Theoretical Model. We write the lateral momentum equation that governs lateral circulation (12, 71)

$$K_{v,z}\frac{\partial^2 v(z)}{\partial z^2} = g\frac{\partial \eta}{\partial y} + \beta g\int_z^0 \frac{\partial S}{\partial y}\mathrm{d}z. \quad [1]$$

Here, $v(z)$ is the lateral (y-direction) velocity component. We first examine the depth-dependent structure of lateral circulation before delving into surface transport processes, as is indicated by the vertical coordinate z inside the parentheses. The term $K_{v,z}$ represents the vertical eddy viscosity, η is water level, S is salinity, and β is the haline contraction coefficient relating salinity to density. Density variations in estuaries are typically dominated by salinity, so the effect of temperature is neglected. We have focused on a dominant balance between the internal frictional stress (left side) and barotropic and baroclinic pressure gradients (right side), neglecting the time rate of change and advection terms. The influences of Earth's rotation, local flow curvature, and wind stress are not considered in this simplified model. We have also assumed a depth-uniform vertical eddy viscosity $K_{v,z}$ and a depth-uniform lateral salinity gradient $\partial S/\partial y$ in order to obtain an analytical solution.

Solving Eq. **1** yields the classical solution for density-driven lateral circulation in estuaries (12)

$$v(z) = \frac{\beta g H^3}{48K_{v,z}}\frac{\partial S}{\partial y}\left\{9\left[1-\left(\frac{z}{H}\right)^2\right]-8\left[1+\left(\frac{z}{H}\right)^3\right]\right\}. \quad [2]$$

Here, H is the water depth. The near-surface lateral velocity is thus given by

$$v(z=0) = \frac{\beta g H^3}{48K_{v,z}}\frac{\partial S}{\partial y}. \quad [3]$$

Henceforth, we will drop off $z = 0$ in the parenthesis and use v to denote the surface lateral velocity.

Next, we consider the equation for the lateral salinity gradient to investigate the baroclinic forcing driving the lateral circulation.

$$\frac{\partial}{\partial t}\frac{\partial S}{\partial y} = -\frac{\partial u}{\partial y}\frac{\partial S}{\partial x} + K_{S,y}\frac{\partial^3 S}{\partial y^3}, \quad [4]$$

This equation is obtained by taking the lateral derivative $\partial/\partial y$ of the salinity transport equation (38). Here, t is time, and u is the velocity component in the along-estuary (x) direction. In Eq. **4**, the lateral salinity gradient is determined by two competing processes, i.e., straining by laterally sheared flow [the first term on the right side, corresponding to the differential advection of salinity that creates lateral gradients (6, 41)] and horizontal mixing that destroys lateral salinity gradients. We have assumed depth-uniform streamwise velocity u and salinity S. The term $K_{S,y}$ is an effective salinity mixing coefficient in the lateral direction. We first focus on a scenario where the lateral structure of salinity can immediately respond to the laterally sheared flow. This is typically true for small and intermediate estuaries where the advection and lateral mixing timescales are small compared to the tidal period (12, 34, 42, 43). Therefore, we can omit the time derivative term in Eq. **4** in this scenario, and write

$$K_{S,y}\frac{\partial^3 S}{\partial y^3} = \frac{\partial u}{\partial y}\frac{\partial S}{\partial x}. \quad [5]$$

We prescribe the tidally varying and laterally sheared surface streamwise velocity as

$$u = \left[u_1 + \frac{\Delta u_1}{2}\cos\left(\frac{2\pi y}{W}\right)\right]\sin\left(\frac{2\pi t}{T}\right) - u_0. \quad [6]$$

The velocity varies sinusoidally in time t with a period of T. The term u_0 is the tidal-mean seaward surface velocity, which includes contributions from both

river flow and estuarine exchange flow. Note that $-u_0 < 0$, which indicates the seaward direction, and we express u_0 as positive values for convenience. The term u_1 is the amplitude of the laterally averaged tidal velocity. The velocity also has lateral variation in a sinusoidal pattern, with its maximum at the centerline ($y = 0$) and minimum at the bank ($y = W/2$, with W being the channel width). The difference between the lateral maximum and minimum of the streamwise velocity amplitude is Δu_1. The velocity difference Δu_1 typically depends on the lateral variability of channel bathymetry (38, 41), and can also be enhanced by the presence of topographic features like headlands and meanders (64, 65). Combining Eqs. **3**, **5**, and **6**, we can explicitly write the surface lateral velocity as

$$v = -v_1 \sin\left(\frac{2\pi y}{W}\right) \sin\left(\frac{2\pi t}{T}\right). \quad [7]$$

The amplitude of the tidally varying surface lateral velocity is given by

$$v_1 = -\frac{\beta g H^3}{48 K_{v,z}} \frac{\partial S}{\partial x} \frac{\Delta u_1 W}{4\pi K_y}. \quad [8]$$

Note that $v_1 > 0$ because $\partial S/\partial x < 0$ in estuaries, with positive x denoting the landward direction. The amplitude of lateral velocity (v_1) depends on various factors, e.g., water depth, the along-estuary salinity gradient, and the lateral shear in streamwise velocity. The expression in Eq. **8** typically applies to well-mixed and weakly stratified estuaries, while in strongly stratified estuaries, the interaction between eddy viscosity $K_{v,z}$ and stratification may lead to additional complexity (12). For comparison with numerical models, v_1 can be readily obtained by applying a sinusoidal fitting to the surface velocity field. This allows us to focus on a kinematic solution for surface particles without delving into the dynamical processes that dictate the value of v_1.

Surface particle transport in the simplified model can therefore be calculated using

$$\begin{aligned} \frac{\mathrm{d}\mathcal{X}}{\mathrm{d}t} &= u, \\ \frac{\mathrm{d}\mathcal{Y}}{\mathrm{d}t} &= v, \end{aligned} \quad [9]$$

where $\mathcal{X}$ and $\mathcal{Y}$ are the along-estuary and lateral locations of the particle. Eq. **9** can be numerically solved when combined with the surface streamwise and lateral velocities (u and v) in Eqs. **6** and **7**. The tidally averaged Lagrangian velocity of surface particles is given by

$$\mathcal{U}_{\mathrm{theo}} = \frac{\mathcal{X}(t = nT) - \mathcal{X}(t = 0)}{nT}, \quad [10]$$

with n being an integer. This theoretical model for particle transport is dependent on three dimensionless parameters, $\Omega W/v_1$, $\Delta u_1/u_1$, and u_0/u_1. Here, $\Omega = 2\pi/T$ is the tidal radian frequency. In particular, the direction of surface particle transport in the model, i.e., landward or seaward, is determined solely by two parameters $\Omega W/v_1$ and $u_0/\Delta u_1$, as illustrated in Fig. 6*D*.

Another scenario derived from Eq. **4** involves a time-varying response in the salinity field while neglecting the horizontal mixing term,

$$\frac{\partial}{\partial t}\frac{\partial S}{\partial y} = -\frac{\partial u}{\partial y}\frac{\partial S}{\partial x}. \quad [11]$$

While an immediate response in the salinity field (Eq. **7**) typically applies to small and intermediate width estuaries, in large estuaries like the Delaware Bay, the creation of lateral salinity gradients may lag the variation in tidal velocity (48), so that the time derivative in Eq. **11** can be dominant. In this scenario, the surface lateral velocity can be written as

$$v = v_2 \sin\left(\frac{2\pi y}{W}\right) \cos\left(\frac{2\pi t}{T}\right), \quad [12]$$

and

$$v_2 = -\frac{\beta g H^3}{48 K_{v,z}} \frac{\partial S}{\partial x} \frac{\Delta u_1 T}{2W}. \quad [13]$$

Note that in Eq. **12**, the lateral circulation lags behind the streamwise velocity (Eq. **6**) in time. This lag in tidal phase between lateral and streamwise velocity will affect the along-estuary transport of surface particles and may contribute to discrepancies between numerical simulations and the theoretical prediction based on Eq. **7**. Including this lagged response (Eq. **12**) in large estuaries still generally results in seaward transport of surface particles, and thus would not change the conclusion obtained from the immediate response scenario (Eq. **7**).

Data, Materials, and Software Availability. The idealized numerical model data supporting this study are available at https://doi.org/10.5281/zenodo.10223457 (84). The North River model data are available at https://doi.org/10.5281/zenodo.8126968 (85). The Delaware Bay model data are available at http://clancy.whoi.edu:8080/thredds/catalog/data1/jchen/delaware/catalog.html (86). The particle tracking data are available at https://doi.org/10.5281/zenodo.10223512 (87). The source code of the ROMS model is available at https://www.myroms.org (88). The source code of the ROMSPath particle tracking model is available at https://github.com/imcslatte/ROMSPath (89).

ACKNOWLEDGMENTS. The research leading to these results was funded by the NSF (OCE-2123002). We thank Adrian Garcia for helpful discussions on the North River estuary and for providing the drone imagery, Elias Hunter for his support with the particle tracking model, and Florent Grasso and Romaric Verney for helpful discussions on the Seine estuary.

1. K. Dyer, *Estuaries: A Physical Introduction, A Wiley-Interscience Publication* (John Wiley, 1973).
2. H. B. Fischer, Mixing and dispersion in estuaries. *Annu. Rev. Fluid Mech.* **8**, 107–133 (1976).
3. J. W. Day Jr., W. M. Kemp, A. Yáñez-Arancibia, B. C. Crump, *Estuarine Ecology* (John Wiley & Sons, 2012).
4. H. K. Lotze *et al*., Depletion, degradation, and recovery potential of estuaries and coastal seas. *Science* **312**, 1806–1809 (2006).
5. P. MacCready, W. R. Geyer, Advances in estuarine physics. *Annu. Rev. Mar. Sci.* **2**, 35–58 (2010).
6. W. R. Geyer, P. MacCready, The estuarine circulation. *Annu. Rev. Fluid Mech.* **46**, 175–197 (2014).
7. V. Klemas, D. Polis, A study of density fronts and their effects on coastal pollutants. *Remote Sens. Environ.* **6**, 95–126 (1977).
8. T. Wang *et al*., Accumulation, transformation and transport of microplastics in estuarine fronts. *Nat. Rev. Earth Environ.* **3**, 795–805 (2022).
9. J. C. Garwood *et al*., Estuarine retention of larvae: Contrasting effects of behavioral responses to turbulence and waves. *Limnol. Oceanogr.* **67**, 992–1005 (2022).
10. E. Summers, J. Du, K. Park, K. Kaiser, How does buoyancy behavior impact microplastic transport in an estuarine environment? *Sci. Total Environ.* **899**, 165687 (2023).
11. H. Burchard, H. M. Schuttelaars, D. K. Ralston, Sediment trapping in estuaries. *Annu. Rev. Mar. Sci.* **10**, 371–395 (2018).
12. R. Nunes, J. Simpson, Axial convergence in a well-mixed estuary. *Estuar. Coast. Shelf Sci.* **20**, 637–649 (1985).
13. J. L. Largier, Estuarine fronts: How important are they? *Estuaries* **16**, 1–11 (1993).
14. J. C. McWilliams, Oceanic frontogenesis. *Annu. Rev. Marine Sci.* **13**, 227–253 (2021).
15. R. Barkan, M. J. Molemaker, K. Srinivasan, J. C. McWilliams, E. A. D'Asaro, The role of horizontal divergence in submesoscale frontogenesis. *J. Phys. Oceanogr.* **49**, 1593–1618 (2019).
16. J. Brown, W. Turrell, J. Simpson, Aerial surveys of axial convergent fronts in UK estuaries and the implications for pollution. *Mar. Pollut. Bull.* **22**, 397–400 (1991).
17. E. Wolanski, W. M. Hamner, Topographically controlled fronts in the ocean and their biological influence. *Science* **241**, 177–181 (1988).
18. D. B. Eggleston, D. A. Armstrong, W. E. Elis, W. S. Patton, Estuarine fronts as conduits for larval transport: Hydrodynamics and spatial distribution of dungeness crab postlarvae. *Mar. Ecol. Progr. Ser.* **164**, 73–82 (1998).
19. A. L. Andrady, Microplastics in the marine environment. *Mar. Pollut. Bull.* **62**, 1596–1605 (2011).
20. M. A. Browne *et al*., Accumulation of microplastic on shorelines woldwide: Sources and sinks. *Environ. Sci. Technol.* **45**, 9175–9179 (2011).
21. M. Cole, P. Lindeque, C. Halsband, T. S. Galloway, Microplastics as contaminants in the marine environment: A review. *Mar. Pollut. Bull.* **62**, 2588–2597 (2011).
22. L. J. Meijer, T. Van Emmerik, R. Van Der Ent, C. Schmidt, L. Lebreton, More than 1000 rivers account for 80% of global riverine plastic emissions into the ocean. *Sci. Adv.* **7**, eaaz5803 (2021).
23. L. C. Lebreton *et al*., River plastic emissions to the world's oceans. *Nat. Commun.* **8**, 15611 (2017).
24. E. Van Sebille *et al*., The physical oceanography of the transport of floating marine debris. *Environ. Res. Lett.* **15**, 023003 (2020).
25. R. Dris, R. Tramoy, S. Alligant, J. Gasperi, B. Tassin, Plastic debris flowing from rivers to oceans: The role of the estuaries as a complex and poorly understood key interface. *Handb. Microplastics Environ.* **1**, 253–280 (2020).

26. S. S. Sadri, R. C. Thompson, On the quantity and composition of floating plastic debris entering and leaving the Tamar Estuary, Southwest England. *Mar. Pollut. Bull.* **81**, 55–60 (2014).
27. P. Vermeiren, C. C. Muñoz, K. Ikejima, Sources and sinks of plastic debris in estuaries: A conceptual model integrating biological, physical and chemical distribution mechanisms. *Mar. Pollut. Bull.* **113**, 7–16 (2016).
28. R. Tramoy, J. Gasperi, L. Colasse, B. Tassin, Transfer dynamic of macroplastics in estuaries-new insights from the seine estuary: Part 1. Long term dynamic based on date-prints on stranded debris. *Mar. pollut. Bull.* **152**, 110894 (2020).
29. R. Tramoy *et al*., Transfer dynamics of macroplastics in estuaries-new insights from the seine estuary: Part 2. Short-term dynamics based on GPS-trackers. *Mar. Pollut. Bull.* **160**, 111566 (2020).
30. T. Van Emmerik, Y. Mellink, R. Hauk, K. Waldschläger, L. Schreyers, Rivers as plastic reservoirs. *Front. Water* **3**, 786936 (2022).
31. C. Brown, S. Holt, G. Jackson, D. Brooks, G. Holt, Simulating larval supply to estuarine nursery areas: How important are physical processes to the supply of larvae to the Aransas Pass Inlet? *Fisher. Oceanogr.* **13**, 181–196 (2004).
32. K. Hunter, P. Liss, Organic matter and the surface charge of suspended particles in estuarine waters. *Limnol. Oceanogr.* **27**, 322–335 (1982).
33. J. Guo, S. Liang, X. Wang, X. Pan, Distribution and dynamics of dissolved organic matter in the Changjiang Estuary and adjacent sea. *J. Geophys. Res. Biogeosci.* **126**, e2020JG006161 (2021).
34. W. M. Kranenburg, W. R. Geyer, A. M. P. Garcia, D. K. Ralston, Reversed lateral circulation in a sharp estuarine bend with weak stratification. *J. Phys. Oceanogr.* **49**, 1619–1637 (2019).
35. T. Bo, D. K. Ralston, W. M. Kranenburg, W. R. Geyer, P. Traykovski, High and variable drag in a sinuous estuary with intermittent stratification. *J. Geophys. Res. Oceans* **126**, e2021JC017327 (2021).
36. R. W. Garvine, R. K. McCarthy, K. C. Wong, The axial salinity distribution in the Delaware estuary and its weak response to river discharge. *Estuar. Coast. Shelf Sci.* **35**, 157–165 (1992).
37. J. L. Chen, D. K. Ralston, W. R. Geyer, C. K. Sommerfield, R. J. Chant, Wave generation, dissipation, and disequilibrium in an embayment with complex bathymetry. *J. Geophys. Res. Oceans* **123**, 7856–7876 (2018).
38. H. B. Fischer, J. E. List, C. R. Koh, J. Imberger, N. H. Brooks, *Mixing in Inland and Coastal Waters* (Elsevier, 1979).
39. T. Bo, D. K. Ralston, A. M. P. Garcia, W. R. Geyer, Tidal intrusion fronts, surface convergence, and mixing in an estuary with complex topography. *J. Phys. Oceanogr.* **54**, 653–677 (2024).
40. J. O'Donnell, Surface fronts in estuaries: A review. *Estuaries* **16**, 12–39 (1993).
41. R. Smith, Longitudinal dispersion of a buoyant contaminant in a shallow channel. *J. Fluid Mech.* **78**, 677–688 (1976).
42. J. R. Lacy, M. T. Stacey, J. R. Burau, S. G. Monismith, Interaction of lateral baroclinic forcing and turbulence in an estuary. *J. Geophys. Res. Oceans* **108**, 3089 (2003).
43. J. A. Lerczak, W. R. Geyer, Modeling the lateral circulation in straight, stratified estuaries. *J. Phys. Oceanogr.* **34**, 1410–1428 (2004).
44. J. Simpson, W. Turrell, *Convergent Fronts in the Circulation of Tidal Estuaries in Estuarine Variability* (Elsevier, 1986), pp. 139–152.
45. A. Valle-Levinson, C. Li, K. C. Wong, K. M. Lwiza, Convergence of lateral flow along a coastal plain estuary. *J. Geophys. Res. Oceans* **105**, 17045–17061 (2000).
46. R. A. Mason, T. Kukulka, J. H. Cohen, Effects of particle buoyancy, release location, and diel vertical migration on exposure of marine organisms to microplastics in Delaware Bay. *Estuar. Coast. Shelf Sci.* **275**, 107990 (2022).
47. A. Valle-Levinson, Density-driven exchange flow in terms of the kelvin and Ekman numbers. *J. Geophys. Res. Oceans* **113**, C04001 (2008).
48. W. R. Geyer, D. K. Ralston, J. L. Chen, Mechanisms of exchange flow in an estuary with a narrow, deep channel and wide, shallow shoals. *J. Geophys. Res. Oceans* **125**, e2020JC016092 (2020).
49. F. Grasso, E. Bismuth, R. Verney, Curviseine hindcast. IFREMER Data Portal (2019). https://doi.org/10.12770/8f5ec053-52c8-4120-b031-4e4b6168ff29. Deposited 10 December 2019.
50. F. Grasso, E. Bismuth, R. Verney, Unraveling the impacts of meteorological and anthropogenic changes on sediment fluxes along an estuary-sea continuum. *Sci. Rep.* **11**, 20230 (2021).
51. T. Mani *et al*., Gaining new insights into macroplastic transport 'hotlines' and fine-scale retention-remobilisation using small floating high-resolution satellite drifters in the chao phraya river estuary of bangkok. *Environ. Pollut.* **320**, 121124 (2023).
52. T. Pokavanich, X. Guo, Saltwater intrusion in chao phraya estuary: A long, narrow and meandering partially mixed estuary influenced by water regulation and abstraction. *J. Hydrol. Reg. Stud.* **52**, 101686 (2024).
53. T. J. Conomos, Movement of spilled oil as predicted by estuarine nontidal drift. *Limnol. Oceanogr.* **20**, 159–173 (1975).
54. J. Gu *et al*., Surface floating objects moving from the pearl river estuary to hainan island: An observational and model study. *J. Mar. Syst.* **241**, 103917 (2024).
55. Z. Chen, M. Bowen, G. Li, G. Coco, B. Hall, Retention and dispersion of buoyant plastic debris in a well-mixed estuary from drifter observations. *Mar. Pollut. Bull.* **180**, 113793 (2022).
56. I. Mazarrasa *et al*., Assessing the risk of marine litter accumulation in estuarine habitats. *Mar. Pollut. Bull.* **144**, 117–128 (2019).
57. K. Bailey *et al*., Quantification and composition of microplastics in the raritan hudson estuary: Comparison to pathways of entry and implications for fate. *Chemosphere* **272**, 129886 (2021).
58. R. Pawlowicz, C. Hannah, A. Rosenberger, Lagrangian observations of estuarine residence times, dispersion, and trapping in the salish sea. *Estuar. Coast. Shelf Sci.* **225**, 106246 (2019).
59. M. Díaz-Jaramillo, M. S. Islas, M. Gonzalez, Spatial distribution patterns and identification of microplastics on intertidal sediments from urban and semi-natural SW Atlantic estuaries. *Environ. Pollut.* **273**, 116398 (2021).
60. L. Ledieu *et al*., Macroplastic transfer dynamics in the loire estuary: Similarities and specificities with macrotidal estuaries. *Mar. Pollut. Bull.* **182**, 114019 (2022).
61. R. Lotcheris *et al*., Plastic does not simply flow into the sea: River transport dynamics affected by tides and floating plants. *Environ. Pollut.* **345**, 123524 (2024).
62. P. M. Tolley, R. R. Christian, Effects of increased inundation and wrack deposition on a high salt marsh plant community. *Estuaries* **22**, 944–954 (1999).
63. T. E. Minchinton, Rafting on wrack as a mode of dispersal for plants in coastal marshes. *Aquat. Bot.* **84**, 372–376 (2006).
64. R. M. McCabe, P. MacCready, G. Pawlak, Form drag due to flow separation at a headland. *J. Phys. Oceanogr.* **36**, 2136–2152 (2006).
65. T. Bo, D. K. Ralston, Flow separation and increased drag coefficient in estuarine channels with curvature. *J. Geophys. Res. Oceans* **125**, e2020JC016267 (2020).
66. A. M. P. Garcia, W. R. Geyer, N. Randall, Exchange flows in tributary creeks enhance dispersion by tidal trapping. *Estuaries Coasts* **45**, 363–381 (2021).
67. R. W. Garvine, A simple model of estuarine subtidal fluctuations forced by local and remote wind stress. *J. Geophys. Res. Oceans* **90**, 11945–11948 (1985).
68. J. H. Cohen, A. M. Internicola, R. A. Mason, T. Kukulka, Observations and simulations of microplastic debris in a tide, wind, and freshwater-driven estuarine environment: The Delaware Bay. *Environ. Sci. Technol.* **53**, 14204–14211 (2019).
69. M. S. Longuet-Higgins, On the transport of mass by time-varying ocean currents. *Deep Sea Res. Oceanogr. Abstr.* **16**, 431–447 (1969).
70. M. Moulton *et al*., Exchange of plankton, pollutants, and particles across the nearshore region. *Annu. Rev. Mar. Sci.* **15**, 167–202 (2023).
71. W. R. Geyer, Three-dimensional tidal flow around headlands. *J. Geophys. Res. Oceans* **98**, 955–966 (1993).
72. R. J. Chant, R. E. Wilson, Secondary circulation in a highly stratified estuary. *J. Geophys. Res. Oceans* **102**, 23207–23215 (1997).
73. T. Kukulka, R. J. Chant, Surface convergence zones due to lagrangian residual flow in tidally driven estuaries. *J. Phys. Oceanogr.* **53**, 423–431 (2023).
74. C. Li, J. O'Donnell, Tidally driven residual circulation in shallow estuaries with lateral depth variation. *J. Geophys. Res. Oceans* **102**, 27915–27929 (1997).
75. A. F. Shchepetkin, J. C. McWilliams, The regional oceanic modeling system (ROMS): A split-explicit, free-surface, topography-following-coordinate oceanic model. *Ocean Model.* **9**, 347–404 (2005).
76. D. B. Haidvogel *et al*., Ocean forecasting in terrain-following coordinates: Formulation and skill assessment of the regional ocean modeling system. *J. Comput. Phys.* **227**, 3595–3624 (2008).
77. A. F. Shchepetkin, J. C. McWilliams, Correction and commentary for "ocean forecasting in terrain-following coordinates: Formulation and skill assessment of the regional ocean modeling system" by haidvogel et al., J. Comp. Phys. 227, pp. 3595–3624. *J. Comput. Phys.* **228**, 8985–9000 (2009).
78. J. C. Warner, B. Armstrong, R. He, J. B. Zambon, Development of a coupled ocean-atmosphere-wave-sediment transport (coawst) modeling system. *Ocean Model.* **35**, 230–244 (2010).
79. L. Umlauf, H. Burchard, A generic length-scale equation for geophysical turbulence models. *J. Mar. Res.* **61**, 235–265 (2003).
80. T. Bo, D. K. Ralston, W. R. Geyer, Sources of drag in estuarine meanders: Momentum redistribution, bottom stress enhancement, and bend-scale form drag. *J. Phys. Oceanogr.* **53**, 1629–1650 (2023).
81. R. A. Luettich, J. J. Westerink, N. W. Scheffner, "ADCIRC: An advanced three-dimensional circulation model for shelves, coasts, and estuaries. report 1, theory and methodology of ADCIRC-2DD1 and ADCIRC-3DL" (Tech. Rep. DRP-92-6, Dredging Research Program, U.S. Army Engineers Waterways Experiment Station, 1992).
82. T. Bo, D. K. Ralston, Frontogenesis, mixing, and stratification in estuarine channels with curvature. *J. Phys. Oceanogr.* **52**, 1333–1350 (2022).
83. E. J. Hunter *et al*., ROMSPath v1.0: Offline particle tracking for the regional ocean modeling system (ROMS). *Geosci. Model Dev.* **15**, 4297–4311 (2022).
84. T. Bo, Idealized estuary model data. Zenodo. https://doi.org/10.5281/zenodo.10223457. Deposited 29 November 2023.
85. T. Bo, North River estuary model data. Zenodo. https://doi.org/10.5281/zenodo.8126968. Deposited 5 November 2021.
86. J. Chen, Delaware estuary model data. WHOI Data Portal. http://clancy.whoi.edu:8080/thredds/catalog/data1/jchen/delaware/catalog.html. Deposited 27 April 2016.
87. T. Bo, Particle tracking data in idealized and realistic estuary models. Zenodo. https://doi.org/10.5281/zenodo.10223512. Deposited 29 November 2023.
88. H. G. Arango, A. F. Shchepetkin, Regional Ocean Modeling System (ROMS). Apache Subversion. https://www.myroms.org. Accessed 10 January 2019.
89. E. J. Hunter, ROMSPath. GitHub. https://github.com/imcslatte/ROMSPath. Accessed 9 March 2023.